UNIVERSITY OF VIRGINIA

MASTERS THESIS

Automated Volumetric Skull Segmentation Utilizing Ultra Short Echo Time Magnetic Resonance Imaging for MRgFUS

Author:
SAMARTH SINGH

Supervisor:
DR. WILSON MILLER

A thesis submitted in partial fulfillment of the requirements for the degree of Master of Science

in the

Miller Lab
Department of Biomedical Engineering

December 5, 2020

Declaration of Authorship

I, SAMARTH SINGH, declare that this thesis titled, "Automated Volumetric Skull Segmentation Utilizing Ultra Short Echo Time Magnetic Resonance Imaging for MRgFUS" and the work presented in it are my own. I confirm that:

- This work was done wholly or mainly while in candidature for a research degree at this University.
- Where any part of this thesis has previously been submitted for a degree or any other qualification at this University or any other institution, this has been clearly stated.
- Where I have consulted the published work of others, this is always clearly attributed.
- Where I have quoted from the work of others, the source is always given. With the exception of such quotations, this thesis is entirely my own work.
- I have acknowledged all main sources of help.
- Where the thesis is based on work done by myself jointly with others, I have made clear exactly what was done by others and what I have contributed myself.

Signed: Samarth Singh

Date: August 3, 2020

"audentis Fortuna iuvat."

Turnus

UNIVERSITY OF VIRGINIA

Abstract

Dr. Wilson Miller
Department of Biomedical Engineering

Master of Science

Automated Volumetric Skull Segmentation Utilizing Ultra Short Echo Time Magnetic Resonance Imaging for MRgFUS

by SAMARTH SINGH

Transcranial Magnetic Resonance guided Focused Ultrasound (tcMRgFUS) is a noninvasive treatment method which involves deposition of sonic energy using ultrasonic beams in the neurocranium region to achieve thermal effects (e.g. tissue ablation, hyperthermia), mechanical effects(e.g. blood-brain barrier permeabilization,clot dissolution, tissue homogenization), and physiological effects (e.g. neuromodulation). The skull, made out of predominantly cancellous and cortical bones, presents itself as an acoustic barrier to this ultrasonic energy. The skull absorbs ultrasound to an extent, heating up and also causing the sonic beams to scatter from the intended target. It is extremely critical from a treatment standpoint to ensure the focal point decided upon for thermal energy deposition is the only region which is sonicated, since the treatment efficacy and outcome depends on the same. Current skull extraction methods involve a prior computed tomography(CT) of the patient undergoing treatment, which provides a bone map for correcting the Focal Ultrasound transducers' phases to ensure accurate energy deposition. Previous work has shown Ultrashort Echo Time(UTE) Magnetic Resonance(MR) imaging allows us to visualize the skull in a patient, and sonication efficacy was improved for tcMRgFUS procedures with accurate, albeit ad-hoc estimation of the skull. In this work, we propose a completely automated volumetric skull extraction algorithm that operates on UTE MR scans of a patient, and extracts the skull utilizing stochastic image modeling and segmentation techniques such as Gaussian mixture modeling, expectation maximization, Markov random fields and least squares optimization.UTE MR volumes were compared with co-registered CT ground truth for 7 subjects who underwent essential tremor (ET) treatment. Dice coefficients varying from 0.721 to 0.817 were obtained.This work has the potential of integration in a clinical workflow for tcMRgFUS treatment, saving costs both in money and time for the patient, while involving zero harmful ionizing X-Ray radiation.

Acknowledgements

I would first like to thank my advisor Dr. Wilson Miller, for being patient with me, and helping me constantly improve as an engineer. Dr. Scott Acton for the guidance and assistance provided at various stages of graduate school, and the coffee hour discussions that I cherish. Dr. Gustavo Rohde for helping me realize how important mathematical models are for the field I intend to pursue my PhD in, and being a fantastic mentor setting mathematical foundations through my MS process. Dr. Shayn Peirce Cottler for giving a glimpse into life as a graduate student, and helping me in adjusting at graduate school - the mock qualifier final exam of Physiology is something I still remember and value. Dr. Craig Meyer for showing faith in me during admissions and helping me in getting accustomed to UVA BME, and connecting me with Dr. Wilson Miller. Dr. Steven Allen, for the important lessons in life in graduate school , and being a good mentor through my time here at UVA.Dr. Daniel Weller for allowing me to present my work to his lab, and also giving critical feedback on my teaching. Dr. Timothy Allen for the good conversations during my TA period with the BME department. Extended gratitude to Dr. Dan and Dr. Changyu for being friends and mentors through my time here.

I would also like to extend my gratitude to my peers, especially Katya Gilbo, Shifat, Quan Dou and Zhixing Wang for helping me learn and be willing to share their knowledge with me. I sincerely value the discussions we had, and those helped me constantly evolve.

Gratitude is obviously extended to family and friends, both in US as well as India.

And finally, thanks Universe, remain kind.

Contents

List of Figures

List of Abbreviations

MRI	**M**agnetic **R**esonance **I**maging
CT	**C**omputed **T**omography
FUS	**F**ocused **U**ltrasound
MRgFUS	**M**agnetic **R**esonance **g**uided **F**ocused **U**ltrasound
tcMRgFUS	**t**rans**c**ranial **M**agnetic **R**esonance **g**uided **F**ocused **U**ltrasound
SDR	**S**kull **D**ensity **R**atio
UTE	**U**ltrashort **E**cho **T**ime
EM	**E**xpectation **M**aximization
MRF	**M**arkov **r**andom **f**ield
GMM	**G**aussian **Mixture M**odel
TR	**R**epitition **T**ime
TE	**E**cho **T**ime

Dedicated to the souls who have helped me along the way, and to the remaining who shall show up in the life that remains. . .

Chapter 1

Introduction

1.1 Transcranial MRgFUS and Clinical Applications

Transcranial Magnetic Resonance guided Focused Ultrasound(MRgFUS) is a minimally invasive treatment approach that involves deposition of sonic energy at a specific target located within the brain. A Magnetic Resonance(MR) image allows a neurosurgeon to target specific tissue sites in the patient, while monitoring in real time, the energy deposition from Focused Ultrasound (FUS), thereby ensuring no harm is caused to neighboring tissues and the patient. By integrating FUS and MRI in a single therapy method, MRgFUS offers a non invasive and safe alternative to surgical resection or radiation therapy of benign and malignant tumors [1].

Depending on the treatment approach, MRgFUS can induce thermal effects (e.g. tissue ablation, hyperthermia), mechanical effects (e.g. blood-brain barrier permeabilization, clot dissolution, tissue homogenization), and physiological effects (e.g. neuromodulation)[2]–[4]

MRgFUS has the potential for treatment and management of a variety of neurological as well as psychiatric disorders[5][6], Fig 1.1 shows transcranial ablation targets along with the specific psychiatric disorders that can be treated. As can be observed, specific ablation targets have the potential of treating/managing specific diseases/disorders.[7]–[9]

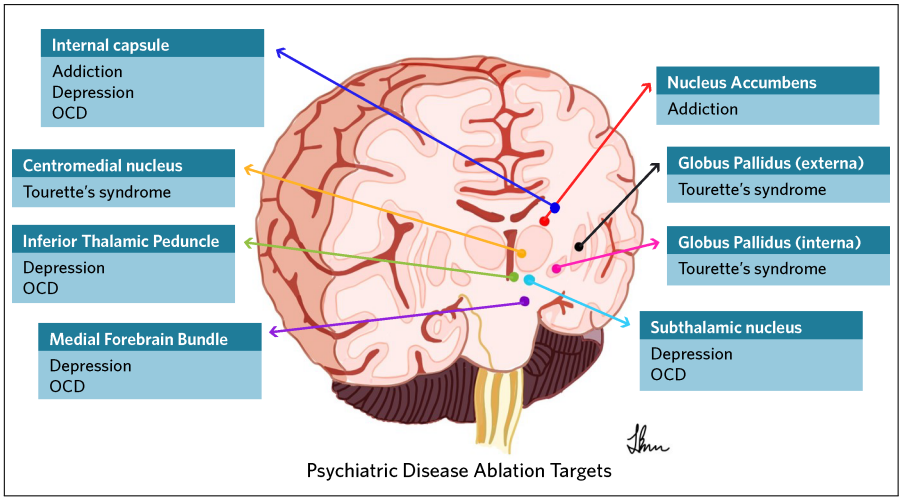

FIGURE 1.1: Psychiatric Disease Ablation Targets : Courtesy FUS Foundation

1.2 Working Principle of MR guided Focused Ultrasound

A typical MRgFUS setup is shown in Fig 1.2 . The sagittal MRI shows the patient's head immersed in a water bath, and surrounded by a hemispherical FUS phased array transducer. The MRI is used for specific targeting of tissue in the brain (depicted by the red spot). During the non invasive procedure, the ablation target is monitored constantly to ensure efficacy of the treatment. The water bath depicted in Fig 1.2 has two roles – it provides a medium for the ultrasound waves to propagate and is used for cooling of the skull during the procedure.

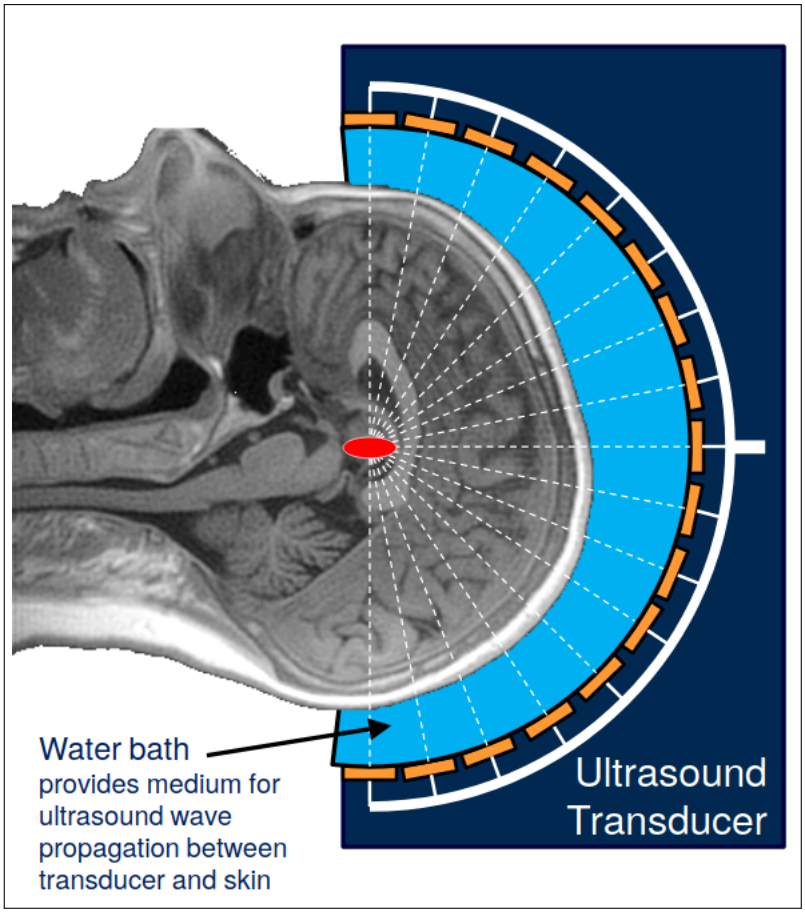

FIGURE 1.2: MRgFUS Setup : A sagittal MR slice of a patient head inserted in a FUS transducer suspended in water bath. The FUS transducers focus ultrasonic beam at a specific target in the neurocranium

The MRgFUS procedure can be used to target tissues for ablation as small as 1x1.5mm to 10x16 mm. [7]

1.3 Transcranial MRgFUS and the Skull – a Challenge

The skull provides an acoustic barrier for the FUS beams to propagate successfully to the tissue target in the brain[8]. The FUS beams are generated using a helmet-shaped hemispherical transducer (Fig 1.3a,1.3b), using between 750 and 1000 individual elements to distribute the ultrasound energy over a large skull surface area. However, the presence of the skull compromises the efficiency of transcranial FUS therapy. The heterogeneous nature and acoustic characteristics of the skull induce significant phase aberrations and energy attenuation, especially at the higher acoustic frequencies employed in transcranial FUS(tcFUS). These aberrations have the potential to distort and shift the acoustic focus of

(A) FUS Transducer : Front View

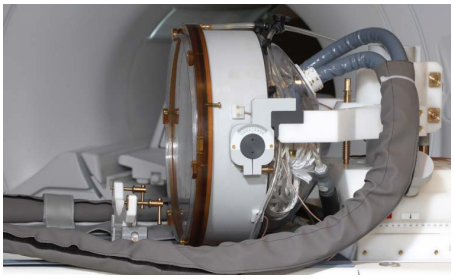

(B) FUS Transducer : Side View

FIGURE 1.3: FUS Transducer

the FUS beams, as well as induce heating at the patient's scalp and outer cortical bone[9] .The individual transducer elements have their phase corrected to account for the heterogeneity of the skull through which the sonic beams traverse[10].
The term 'calvaria' is used to describe the upper part of the neurocranium (brain cavity). Transcranial FUS beams must be focused through the calvaria at the thermal energy deposition target. The correction in phase of the individual FUS transducer elements depends on accurate knowledge of the geometrical arrangement of bone in the beam path. Currently, CT scans taken prior to MRgFUS treatment are used to construct the required bone maps. Another important metric is the skull density ration (SDR), which is the global average of the ratio between the radiodensity in CT Hounsfield units of cancellous to cortical bone within the calvaria[11].

1.4 Using MRI for imaging the Skull

In current MRgFUS procedures, a bone map for the patient is obtained using CT. Based on this bone map, the FUS transducers' phase is adjusted to ensure accurate deposition of energy at the desired focal point. The use of CT exposes the patient to ionizing radiation, besides adding time and cost to the treatment.
Magnetic Resonance Imaging has been traditionally used to observe soft tissues within the human body. Recent advancements in pulse sequence development have allowed researchers to observe harder tissues (bone, tendon,ligaments) efficiently, utilizing a clinically compatible pulse sequence called Ultra Short TE sequence[12]. Fig 1.4 represents a series of images with varying contrasts acquired using a UTE Dual Echo pulse sequence from the Miller Lab.
The UTE pulse sequence yields two inherently co-registered 3D image sets : one at ultrashort echo time having non-zero bone signal (short TE) Fig 1.4 **a**), and the other at a longer echo time having near-zero bone signal Fig 1.4 **b**). The

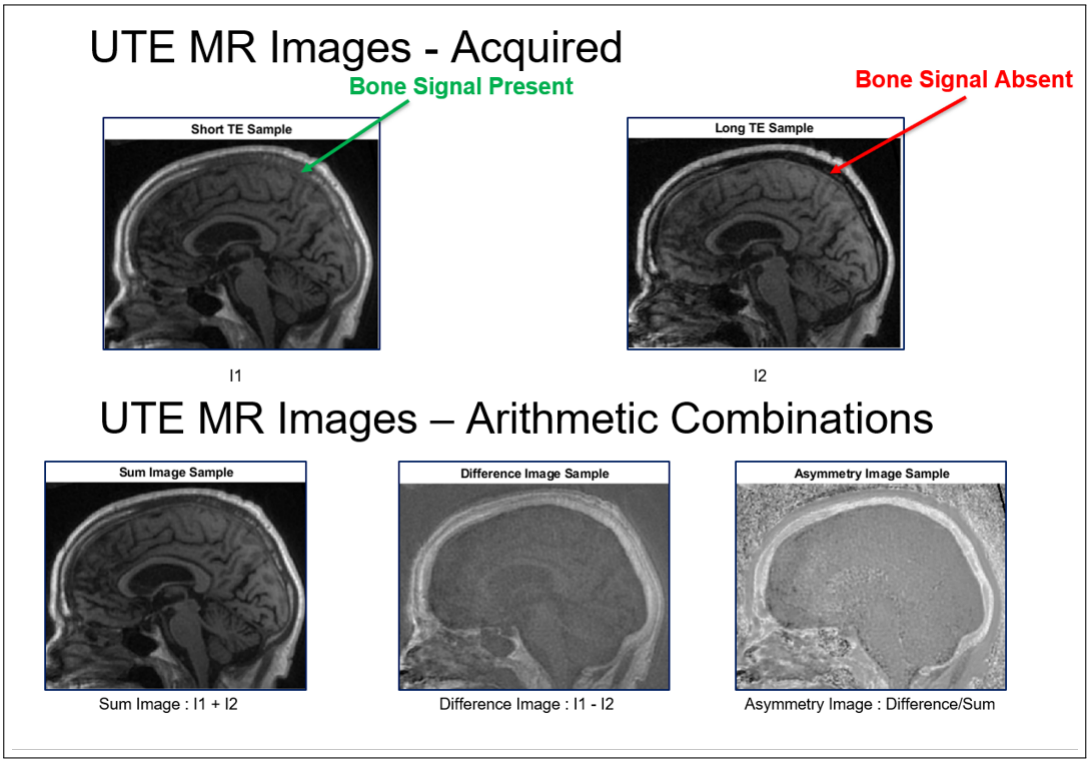

FIGURE 1.4: UTE MR Sagittal images utilized for algorithm. Short TE image is I1, Long TE image is I2. Arithmetic combinations are further shown, with the skull becoming visible as a bright white rind in asymmetry image

difference between these images shows bright bone signal but also highlights subcutaneous fat in the scalp Fig 1.4 **c**) . Dividing the difference by the sum (Diff/Sum), the asymmetry image volume suppressed the fat signal, enhancing bone conspicuity Fig 1.4 **d**).
A single clinical workflow could be incorporated if the MR system used for guidance in FUS procedures is also used for generating a bone map for the patient using UTE imaging - thereby ensuring the patient does not get exposed to ionizing radiation, and also saves on time and money on the MRgFUS procedure.Furthermore, with a bone map available, aberration correction for FUS procedures would be performed more efficiently. This would eventually lead to a much more efficient and streamlined clinical outcome for the patient and the healthcare provider.

1.5 An Automated Skull Extraction Algorithm

By integrating a UTE MRI pre-scan in the MRgFUS clinical workflow, we hypothesize that accurate representations of the skull can be obtained (as shown in Fig 1.4 **a**) – **d**)). An automated volumetric skull extraction algorithm can be integrated on the MRgFUS system itself, providing a skull map, which could be used for accurately correcting the phase of each individual element in the FUS transducer. This would enhance patient comfort by ensuring harmful ionizing radiation dose is reduced to zero, and also provide a single clinical workflow for the patient and the caregiver.
In this thesis, we present a volumetric skull extraction algorithm developed utilizing MATLAB (The Mathworks, Natick, MA) that is completely automated. It utilizes different contrasts made available from a UTE Dual Echo pulse sequence developed in the Miller Lab @ UVA, and yields a skull map which is compared with co-registered CT data. We tested our algorithm on seven different subjects who previously underwent essential tremor (ET) treatment. We provide DICE coefficients as a metric to discuss our current accuracy obtained compared to the CT ground truth, and present viewpoints on further improvements that can be incorporated to ensure efficacy of this algorithm for use on a regular basis on clinical MRgFUS systems.

Chapter 2

Data Acquisition

2.1 The MRgFUS System used

As mentioned previously, the MRgFUS consists of two important hardware components – an MRI system for "guidance" and a Focused Ultrasound system for sonic energy deposition. This integrated system is shown in Fig 2.1

FIGURE 2.1: MRgFUS System : Insightec ExAblate Neuro 4000 integrated with GE 1.5T MRI Scanner

An Insightec ExAblate® Model 4000 neurosurgery platform (FUS system) available at the UVA Health System was used for the MRgFUS treatment for the 8 subjects. The FUS transducer is a phased array, piezoceramic helmet with 1024

elements operating at a frequency of 650 kHz. The caregiver can utilize this system to focus ultrasound at transcranial locations as minute as 2-5 mm, with a focal accuracy of <1 mm [13]. This system utilizes a GE Signa 1.5T MRI Scanner for image guidance.
The images used for this thesis were obtained using the Siemens Trio 3T Scanner in the Snyder Building at the Fontaine Research Park, Charlottesville, Virginia, The United States of America. An ultrashort dual echo UTE sequence developed at the Miller Lab was run on the scanner to obtain the volumetric dataset for the development of the automated skull extraction algorithm

2.2 MRI Pulse Sequence used for Skull Imaging

A 3D dual echo UTE pulse sequence with radial acquisition was used with echo times(TE) of 0.8ms and 2.5ms. This pulse sequence is depicted in Fig 2.2

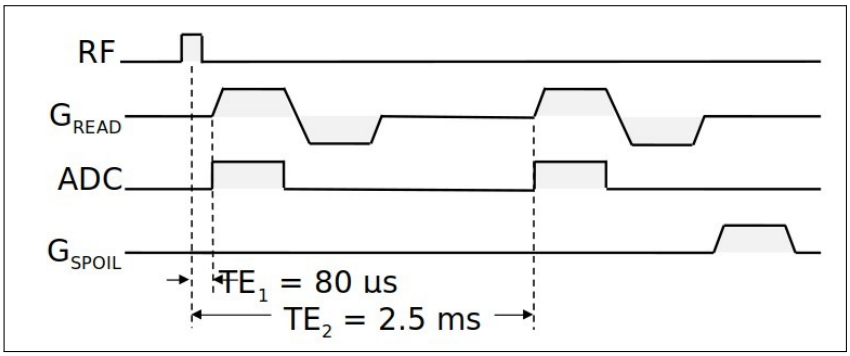

FIGURE 2.2: Dual Echo UTE Pulse Sequence : Courtesy Miller Lab

A UTE sequence in MRI is a steady state spoiled incoherent gradient echo sequence with very short repetition time TR. The signal in a voxel for a volume collected using this pulse sequence is given by [14]

$$\hat{\rho}(\theta, T_E) = \rho_0 \sin(\theta) \frac{(1 - E_1)}{1 - \cos(\theta) E_1} E_2 \tag{2.1}$$

where

$$E_1 = \exp(\frac{-TR}{T1})$$

and

$$E_2 = \exp(\frac{-T_E}{T_2^*})$$

In the above equation, $\hat{\rho}(\theta, T_E)$ indicates the voxel signal intensity as a function of echo time and flip angle (longitudinal magnetization is 'flipped' into the

transverse plane by an amount proportional to the sine of this angle) applied by the RF pulse. ρ_0 represents voxel spin density. There are four terms related to time, which lay the foundation of signal evolution in MRI. These terms are pulse repetition time TR (entire duration of the block shown in Fig 2.2), T1 (physical time constant representing exponential rate of longitudinal magnetization recovery in MR), $T2^*$ (physical time constant representing exponential decay of transverse magnetization due to spin-spin interactions and magnetic field inhomogeneities) and echo time TE (time at which signal is sampled). T1 and $T2^*$ depend on the tissue type as well as the scanner field strength(1.5T or 3T generally). In a dual echo UTE pulse sequence, as described in Fig 2.2 , 'dual' implies the signal emanating from tissues is sampled twice, at two different echo times. When TR<5T1 [15], the signal gets T1 weighted. Therefore, UTE MR images are T1 weighted inherently. However, bone has a very short $T2^*$, which necessitates 'ultra short' echo times to sample the signal. An illustration of the same can be better understood from Fig 1.4. In Fig 1.4 **a**), the TE is short, and bone and fat appear to have similar intensity(due to T1 weighting). However, at the longer TE, bone signal dies out,whereas fat remains bright. It is this unique contrast between bone and the rest of the tissues that allows arithmetic combinations to yield visually appealing cranium maps, comparable to CT (which is considered the ground truth in modern clinical applications for bone)
This pulse sequence is advantageous to use since it provides two co-registered images with multiple contrasts, specifically between bone and rest of the tissues in the head. The shorter of the two echoes yields high signal from bone, whereas the longer echo time yields 0 bone signal as can be observed from Fig 1.4 **b**) in Section 1.4

2.3 The Dataset

Seven subjects who underwent ET treatment were also scanned using the dual echo UTE sequence depicted in Fig 2.2. Besides the MRI scan, these patients had also undergone a prior CT scan to ensure accurate cranium estimation for their treatment. Therefore, our final dataset included seven UTE MRI volumes which were co-registered with seven CT scans. Fig 2.3 represents the co-registered UTE MRI data with the CT data along axial, sagittal and coronal dimensions.

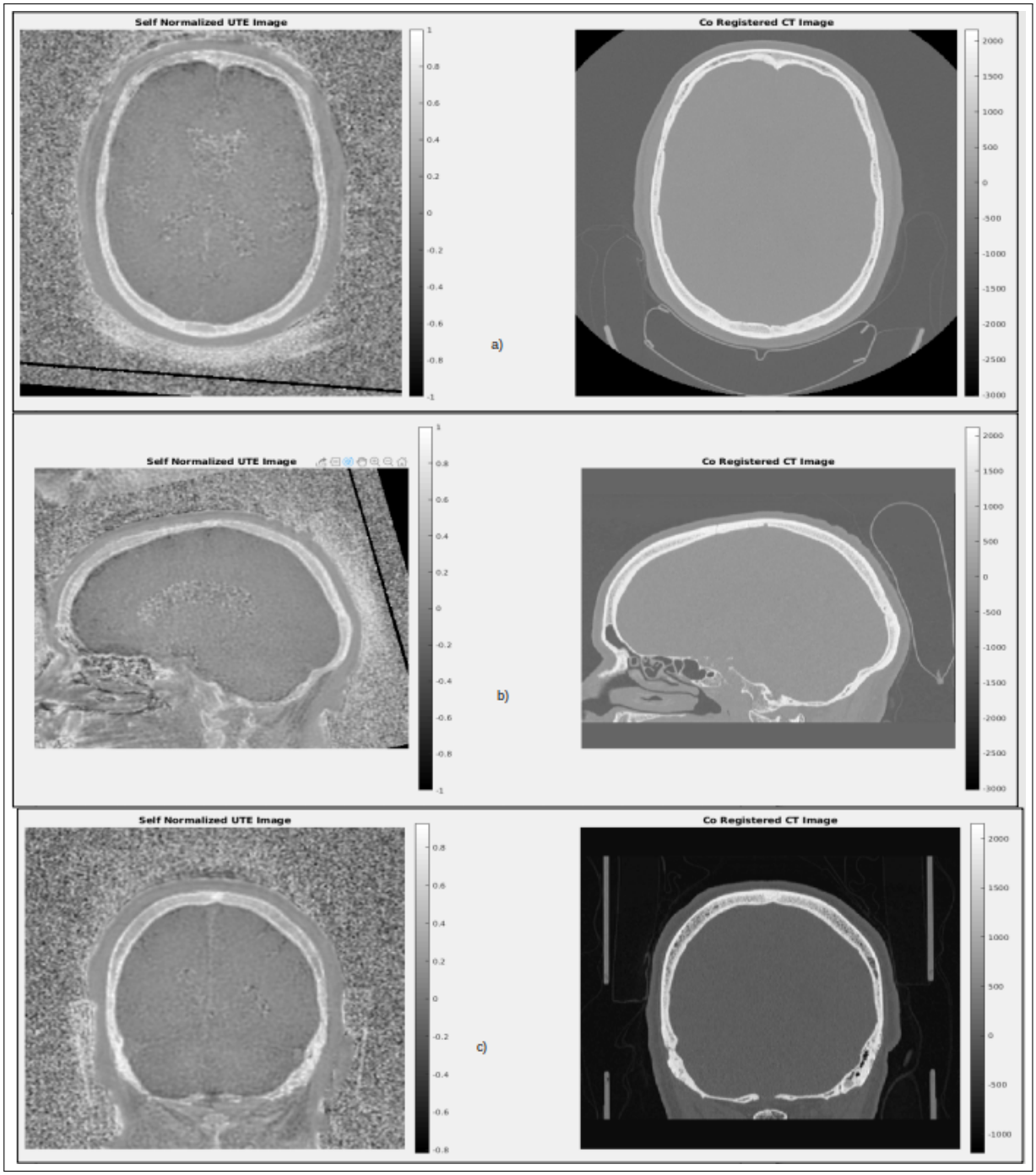

FIGURE 2.3: 3D Volumetric UTE MR Data : Axial, Sagittal and Coronal Slices depicted from a) through c)

Chapter 3

The Automated Volumetric Segmentation Algorithm

3.1 Challenges in Segmentation of UTE MR Volume Images

The signal intensity measured from homogeneous tissue using MRI is seldom uniform. This intensity inhomogeneity arises due to poor RF coil uniformity[16], gradient-driven eddy currents, and patient anatomy both inside and outside FOV. While these intensity inhomogeneities (ranging from 10-20%) have minimal impact on visual diagnosis, the performance of automated segmentation techniques which assume homogeneity of intensity within each tissue type can be significantly degraded[17].
The current dataset was collected using a 16 channel head coil. The spatial sensitivity of the coils plays a key role in estimating the intensity inhomogeneity that arises in MR images, since tissues of same type can appear bright or dark depending on which coil was most sensitive spatially to its presence. Fig 3.1 depicts two major challenges in the segmentation of UTE MR image volumes : intensity inhomogeneity, and bone intensity matching background noise in asymmetry image.

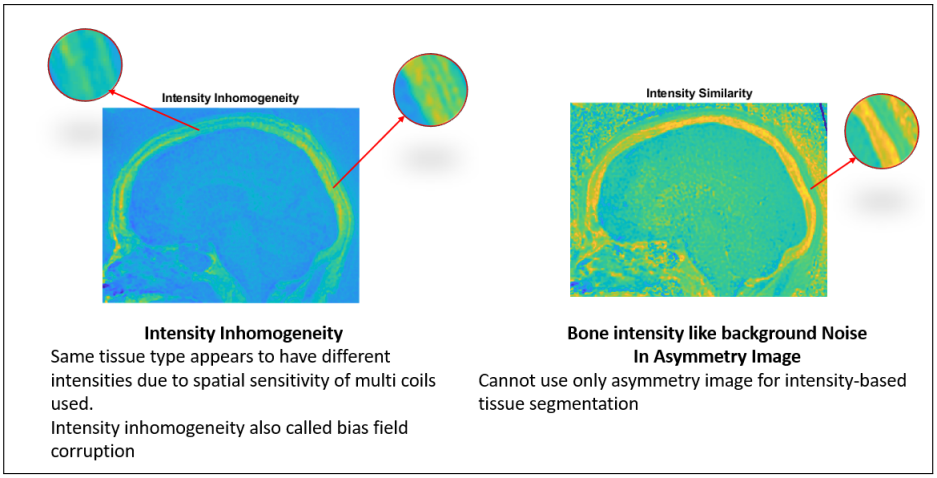

FIGURE 3.1: Two major challenges in UTE MR image volume skull segmentation

The intensity non-uniformity indicates that same tissue types (which are expected to have same tissue intensity due to signal evolution in an MR image) have variable intensity depending on their spatial location. This could lead to errors in algorithms which do not correct this intensity inhomogeneity and utilize histogram based segmentation methods.

3.2 Mathematical Model of MR Image Volumes with Intensity Inhomogeneities

As discussed in Section 3.1 , MR images suffer from intensity inhomogeneity variation due to varying spatial sensitivities of multiple coils used for acquisition of data. This intensity inhomogeneity is generally modeled as a multiplicative field that systematically corrupts the underlying signal[18], which is the desired MR Image Volume. This mathematical model is given by Equation 3.1

$$I(\mathbf{r}) = B(\mathbf{r})J(\mathbf{r}) + \eta(\mathbf{r}) \tag{3.1}$$

where $\mathbf{r} \in \mathbb{R}^3$ is the set of voxels present in the image volume.$I(\mathbf{r})$ represents the observed image volume, $B(\mathbf{r})$ represents the bias field, modeled as a smoothly varying function over space $\mathbf{r}$, $J(\mathbf{r})$ is the desired image volume, and $\eta(\mathbf{r})$ is the additive white Gaussian noise. The measurement of $B(\mathbf{r})$ is challenging and time consuming in real time, requiring phantom calibrations, multicoil spatial sensitivity analysis and also special pulse sequence designs[19]. Therefore, we decided to proceed with estimation of $B(\mathbf{r})$ using underlying statistics of the data obtained. Our algorithm combines stochastic image modeling techniques such as Gaussian mixture models and least squares optimization for estimating tissue intensity in K classes and Markov random fields to incorporate spatial

constraints on the tissue class assignment. The following assumptions about MR images have been made, which are reasonable in context of data available[20].

- MR Images are theoretically piecewise constant with a small number of classes. This implies that the signal arising from tissues of same type must be same (as the signal is dependent on tissue properties itself, as described in Section 2.2) , and the total number of tissues available in an MR image are finite (as there are finite tissue types within the human anatomy).
- High contrast availability between different tissues (in this case specifically bone and not bone) allows segmentation algorithms to function efficiently. An example of the variety of contrasts available with Ultra Short TE MRI has been depicted in Fig 1.4 **a**)-**d**) . By carefully choosing echo time in the pulse sequence design, signal from a variety of tissues can be obtained with appropriate contrast based on eventual requirements.

3.3 Mathematical Derivations for the Algorithm

Restating the problem mathematically from Equation 3.1(each term has been defined in Section 3.2)

$$I(\mathbf{r}) = B(\mathbf{r})J(\mathbf{r}) + \eta(\mathbf{r})$$

We consider five types of image volumes for each subject, which are listed below. Sagittal slices referring to these image volumes have been displayed in Fig 1.4. It is important to note only two of these five image volumes are physically acquired. The other three are obtained through arithmetic combinations.

- I1 : Short TE of the Dual Echo UTE sequence, fat and bone both have non-zero signal at ultra short echo times.
- I2 : Long TE of the Dual Echo UTE sequence, fat still has non zero signal while bone has zero signal due to an extremely short T2*.
- I3 : Sum of I1 and I2, increased SNR due to signal averaging principles.
- I4 : Difference of I1 and I2, fat and bone are the only tissues with bright signal.
- I5 : Self normalized image volume obtained by dividing I4 by I3. Yields an appreciable non zero signal in the skull, visually comparable to CT. Observing this image volume, it becomes essential to separate the bone from fat tissue.

The bias field $B(\mathbf{r})$,as mentioned in Section 3.2, is a smoothly varying spatial field. A popular approach used for correcting this bias field[21] utilized B-splines to estimate this smooth variation, a form of polynomial interpolation. Another approach utilized to measure this smoothly varying spatial field is Legendre's Polynomials, as used by Li. et al. in [22].
The current implementation of our algorithm uses B-spline approximations for estimating the smoothly varying spatial field in a cuboid 3D space (all three dimensions available from the 7 subjects are unequal to each other). An important point to be noted is that I5 does not require bias field estimation since the bias field term gets cancelled in the division process.
The algorithm for skull extraction in the image volumes utilized two separate steps.In the first step, bias field estimation and correction was performed to get an initial segmentation comprising of only bone and fat tissue from the skull image volume. The clique potentials (as described in Section 3.3.8 were not utilized. An energy function, F_1 (explained later in Section 3.3.4 was formulated for Pass 1 of this algorithm.
However, Pass 2 of the algorithm did not utilize bias field correction estimation. Instead, only clique potential estimation (explained in Section 3.3.8) was performed to ensure majority of the skull could be included in our segmentation algorithm. The energy function for this step of the algorithm was formulated as F_2 and has been expounded upon in Section 3.3.9.

3.3.1 Important Definitions

- Ω : Domain over which tissue classes are defined.
- $\mathbf{r} \in \mathbb{R}^3$: Set of voxels before first pass of algorithm - includes both skull and brain.
- $\mathbf{r}_f \in \mathbb{R}^3$: Set of voxels before second pass of algorithm - includes only fat and bone tissue extracted post first pass.
- I($\mathbf{r}$) : Acquired image volume using UTE MRI - corrupted by bias field.
- B($\mathbf{r}$) : Smoothly varying Bias field which leads to intensity inhomogeneity corruption. Modeled linearly.
- J($\mathbf{r}$) : Desired/true image volume, without intensity inhomogeneity correction. Modeled linearly.
- K : Number of tissue classes present in the image.
- i : i-th class of 'K' classes.
- c_i : scalar representing mean tissue intensity of all voxels $\in$ i-th class.
- $\mathbf{c}$: Vector containing 'K' mean tissue intensities.

- $u_i(\mathbf{r})$: binary value representing membership of a voxel to i-th class. Equals 1 when voxels belong to i-th class.
- $\mathbf{u}(\mathbf{r})$: Vector containing voxel membership values defined over Ω.
- G : Column vector valued function representing basis functions for modeling bias field B. First order B- Splines defined over Ω considered in this thesis.
- M : Total number of basis functions used to model bias field B.
- $w_j(\mathbf{r})$: Optimal coefficient for 'j' out of M basis functions.
- $\mathbf{w}$: row vector containing M coefficients for the basis functions defined in G.
- σ_i : Standard deviation of voxel intensities in i^{th} class, where $i \in k, \forall k = 1, 2...K$.
- $F_1(\mathbf{u},\mathbf{c},\mathbf{w})$: Energy function to be optimized for first pass of the algorithm.
- $S_j(\mathbf{r})$: Segmented image volume with 'K' tissues at j^{th} iteration.
- $F_2(\mathbf{u},\mathbf{c})$: Energy function to be optimized for the second pass of the algorithm. This function does not depend on bias field B.

3.3.2 Modeling True Image Volume J

The piecewise approximately constant property of the true image volume J allows the following modeling. $J(\mathbf{r})$ is approximately a constant c_i for $\mathbf{r}$ in i -th tissue class. Let u_i represent membership function for each voxel such that $u_i = 1 \; \forall$ $\mathbf{r} \in$ i-th class and $u_i = 0 \; \forall \; \mathbf{r} \notin$ i-th class. The true image volume can therefore be approximated in matrix form as

$$\mathrm{J}(\mathbf{r}) = \sum_{i=1}^{K} c_i u_i(\mathbf{r}) \tag{3.2}$$

3.3.3 Modeling Bias Field B

The bias field $B(\mathbf{r})$, as mentioned in Section 3.2, is a smoothly varying spatial field. Piecewise polynomials can be utilized to model this smooth variation. M total B-splines are used for estimating the smoothly varying spatial field. Let this set of B-splines be represented by a column vector valued function $G(\mathbf{r}) = g_1 \dots g_M$ The estimation of the bias field is performed by finding the optimal coefficients $w_1 \dots w_M$ in the linear combination $\mathrm{B}(\mathbf{r}) = \sum_{k=1}^{M} w_k g_k$. Therefore, in matrix form, $\mathrm{B}(\mathbf{r})$ can be represented as

$$\mathrm{B}(\mathbf{r}) = \mathbf{w}^T G(\mathbf{r}) \tag{3.3}$$

3.3.4 Modeling Energy Function F_1 for Pass 1

The energy function F_1 is modeled as a Gaussian mixture, which is optimized in a least squares sense.

$$F_1(\mathbf{u},\mathbf{c},\mathbf{w}) = \exp[-\sum_{\mathbf{r}}\sum_{i=1}^{K}\{\frac{[I(r)-\mathbf{w}^T G(r)c_i]u_i(r)}{\sqrt{2}\sigma_i}\}^2] \tag{3.4}$$

By taking the negative natural logarithm, Equation 3.4 can be rewritten with only the argument of the exponential function considered, as follows:

$$-\ln F_1(\mathbf{u},\mathbf{c},\mathbf{w}) = [\sum_{\mathbf{r}}\sum_{i=1}^{K}\{\frac{[I(r)-\mathbf{w}^T G(r)c_i]u_i(r)}{\sqrt{2}\sigma_i}\}^2] \tag{3.5}$$

Optimization of argument of Equation 3.5 leads to deterministic solutions for voxel membership values $\mathbf{u}$, vector containing K mean tissue intensities and also the optimal coefficients for modeling the smoothly varying spatial bias field $\mathbf{w}$, as proposed in [22]. We have introduced Gaussian mixture model optimization to the energy function proposed in [22].It is important to note that maximizing energy as in 3.5 has the same effect as minimizing the energy in 3.4. This energy function is convex in each of its variables $\mathbf{u}$, $\mathbf{c}$ and $\mathbf{w}$, as defined in Section 3.3.1.

3.3.5 Deterministic solution for binary membership u

The following equation must be solved in order to obtain a deterministic solution for $\mathbf{u}$.

$$\arg\max_{\mathbf{u}}[-\ln F_1(\mathbf{u},\mathbf{c},\mathbf{w})] \tag{3.6}$$

Differentiating argument of Equation 3.5 w.r.t $\mathbf{u}$ and equating to 0 yields deterministic solution for $\mathbf{u}$

$$\frac{\partial[\ln F_1(\mathbf{u},\mathbf{c},\mathbf{w})]}{\partial\mathbf{u}} = \frac{\partial[\sum_{\mathbf{r}}\sum_{i=1}^{K}\{\frac{[I(r)-\mathbf{w}^T G(r)c_i]u_i(r)}{\sqrt{2}\sigma_i}\}^2]}{\partial\mathbf{u}} = 0$$

$$\implies \sum_{\mathbf{r}}\frac{\partial\{[(I(r)-\mathbf{w}^T G(r)c_i)u_i(r)]^2\}}{\partial\mathbf{u}} = 0$$

Applying the product rule of differential calculus yields the following (terms that are reduced to zero have not been represented)

$$\implies \sum_{\mathbf{r}} 2[(I(r)-\mathbf{w}^T G(r)c_i)^2 u_i(r)] = 0 \tag{3.7}$$

From Equation 3.7, the following solutions for u_i satisfy

$$u_i(r) = \begin{cases} 1 & i = i_{max}(r) \\ 0 & i \neq i_{max}(r) \end{cases} \tag{3.8}$$

where r represents a single voxel $\in \mathbf{r}$.

3.3.6 Deterministic solution for mean tissue intensity c

The following equation must be solved in order to obtain a deterministic solution for **c**:

$$\arg\max_{\mathbf{c}}[-\ln F_1(\mathbf{u}, \mathbf{c}, \mathbf{w})] \tag{3.9}$$

Introducing bias field B, differentiating argument of Equation 3.5 w.r.t c_i and equating to 0 yields deterministic solution for **c**

$$\frac{\partial[-\ln F_1(\mathbf{u}, \mathbf{c}, \mathbf{w})]}{\partial c_i} = \frac{\partial[\sum_{\mathbf{r}} \sum_{i=1}^{K} \{\frac{[I(r) - B(r)c_i]u_i(r)}{\sqrt{2}\sigma_i}\}^2]}{\partial c_i} = 0$$

The equation above must hold true for all 'i's' . Therefore, rewriting the above

$$\implies \sum_{\mathbf{r}} \frac{\partial[\{\frac{[I(r) - B(r)c_i]u_i(r)}{\sqrt{2}\sigma_i}\}^2]}{\partial \mathbf{c}} = 0$$

$$\implies \sum_{\mathbf{r}} 2(I(r) - B(r)\hat{c_i})(-B(r))u_i(r) = 0$$

$$\implies \sum_{\mathbf{r}} [-2I(r)B(r) + 2B^2(r)\hat{c_i}]u_i = 0 \tag{3.10}$$

Rearranging terms in Equation 3.10 yields

$$\hat{c_i} \sum_{\mathbf{r}} B^2(r)u_i = \sum_{\mathbf{r}} I(r)B(r)u_i$$

Therefore,

$$\hat{c_i} = \frac{\sum_{\mathbf{r}} I(r)B(r)u_i}{\sum_{\mathbf{r}} B^2(r)u_i} \tag{3.11}$$

3.3.7 Deterministic solution for the optimal weights w for the basis functions

The following equation must be solved in order to obtain a deterministic solution for **w**:

$$\arg\max_{\mathbf{w}}[-\ln F_1(\mathbf{u},\mathbf{c},\mathbf{w})] \tag{3.12}$$

$$\frac{\partial[-\ln F_1(\mathbf{u},\mathbf{c},\mathbf{w})]}{\partial \mathbf{w}} = \frac{\partial[\sum_{\mathbf{r}}\sum_{i=1}^{K}\{\frac{[I(r)-\mathbf{w}^T G(r)c_i]u_i(r)}{\sqrt{2}\sigma_i}\}^2]}{\partial \mathbf{w}} = 0$$

$$\implies \sum_{\mathbf{r}}\sum_{i=1}^{K}\frac{\partial[\{\frac{[I(r)-\mathbf{w}^T G(r)c_i]u_i(r)}{\sqrt{2}\sigma_i}\}^2]}{\partial \mathbf{w}} = 0$$

$$\implies \sum_{\mathbf{r}}\sum_{i=1}^{K}\frac{\partial[\{\frac{[I(r)-G^T(r)\mathbf{w}c_i]u_i(r)}{\sqrt{2}\sigma_i}\}^2]}{\partial \mathbf{w}} = 0$$

$$\implies \sum_{\mathbf{r}}\sum_{i=1}^{K}[2(I(r)-G^T(r)\mathbf{w}c_i)(-G^T(r)c_i)u_i(r)] = 0$$

$$\implies -2\sum_{\mathbf{r}}[I(r)G^T(r)(\sum_{i=1}^{K}c_i u_i(r)))] + 2\sum_{\mathbf{r}}\mathbf{w}^T G(r)G^T(r)(\sum_{i=1}^{K}c_i^2 u_i(r)) = 0 \tag{3.13}$$

Let

$$v = \sum_{\mathbf{r}}[I(r)G^T(r)(\sum_{i=1}^{K}c_i u_i(r)))]$$

$$A = \sum_{\mathbf{r}}\mathbf{w}^T G(r)G^T(r)(\sum_{i=1}^{K}c_i^2 u_i(r))$$

Substituting the above values of A and v in Equation 3.13,

$$-2v(\mathbf{r}) + 2A(r)\mathbf{w} = 0$$

$$\mathbf{w} = A^{-1}v(\mathbf{r}) \tag{3.14}$$

The estimated bias field then becomes,

$$B = \mathbf{w}^T G(\mathbf{r}) \tag{3.15}$$

3.3.8 Modeling Clique Potentials using Markov Random Fields for Pass 2

Neighborhood information for each voxel is incorporated in the segmentation process by utilizing Markov random field in the second pass of the algorithm. If N_s is the neighborhood of the voxel at position s $\in \mathbf{r}_f$, then if $S(r_f)$ represents segmentation, the following holds true

$$p(S(\mathbf{r}_f)_s|S(\mathbf{r}_f)_q, \forall\, q \neq s) = p(S(\mathbf{r}_f)_s|S(\mathbf{r}_f)_q, \forall\, q \in N_s) \tag{3.16}$$

26 neighborhood voxels are considered, except at the edges of the image volume, where voxels outside the image volume FOV are not considered. According to the Hammersley-Clifford theorem[23], the probability density of $S(r_f)$ is given by a Gibbs density which has the following form:

$$p(S(\mathbf{r}_f)) \propto \exp(-\sum_C V_c(\mathbf{r}_f)) \tag{3.17}$$

The summation is performed over all cliques , C. A clique is a set of points that are neighbors of each other. The clique potentials V_c depend only on the pixels that belong to clique C. We only consider two-point cliques, which implies, we considered only a pair of points (the voxel under consideration, and its immediate neighbor across three levels of connectivity in the image volume). We define the function V_c $(\mathbf{r}_f)$ as follows:

$$V_c(\mathbf{r}_f) = \begin{cases} -\beta & S(\mathbf{r}_f)_s = S(\mathbf{r}_f)_q, (s,q) \in C \\ +\beta & S(\mathbf{r}_f)_s \neq S(\mathbf{r}_f)_q, (s,q) \in C \end{cases} \tag{3.18}$$

The parameter β is positive, so that two neighboring voxels (3D connectivity of 26 considered) are more likely to belong to the same class than to different classes. It is the formulation of clique potentials in Equation 3.17, and the removal of bias field estimation in second pass of the algorithm that neatly combines with Equation 3.4 to yield the energy function used.

3.3.9 Modeling Energy Function F_2 in Pass 2

$$F_2(\mathbf{u}, \mathbf{c}) = \exp[-\sum_{\mathbf{r}_f}\sum_{i=1}^{K}\{\frac{(I(r_f) - c_i)u_i(r_f)}{\sqrt{2}\sigma_i}\}^2 - \sum_C V_c(\mathbf{r}_f)] \tag{3.19}$$

The method for obtaining deterministic solutions for the above equation remain the same as Pass 1, with two major differences being:

1) The penalty term introduced by the clique potential.

2) The lack of a bias correction term.

3.4 Flowchart of the Algorithm

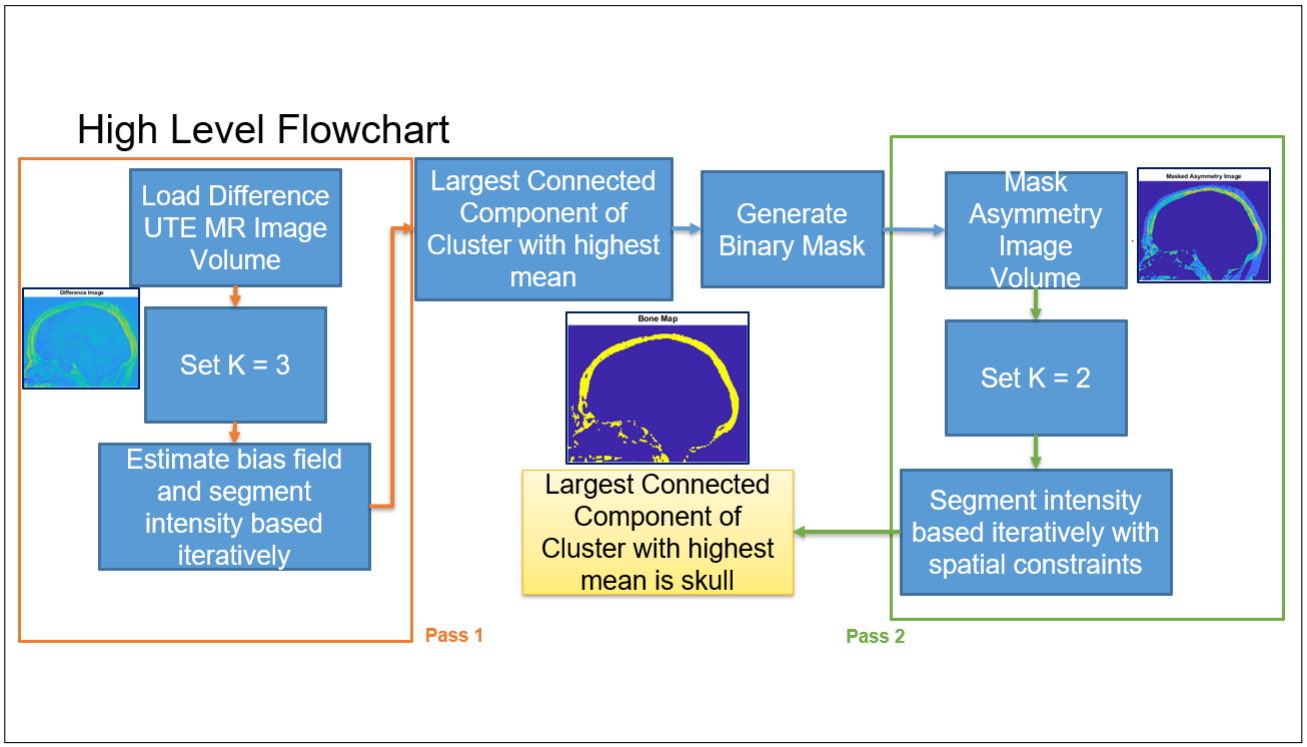

FIGURE 3.2: Flowchart of Algorithm

3.5 Reasoning Behind the Algorithm

The reasoning behind specific steps taken in the algorithm first and second pass are explained below.
1) First Pass:

- In UTE difference image volume I4 (as defined in 3.2, fat and bone pixels have similarly bright intensity,muscle and brain tissue are similarly dim, and air pixels are essentially zero. Therefore, a three - class segmentation is appropriate, and the brightest class will contain primarily fat and bone pixels
- The signal distribution within each class is observed to be well approximated by a Gaussian function. Therefore, Gaussian mixture models are more appropriate to segment rather than Euclidean distance minimization approaches as K-means in this case.
- UTE difference image volume I4 is subject to bias field, and hence estimating and correcting for the same yields a better foreground mask for bone voxels.

- The aim of first pass is to generate an overcomplete segmentation. Therefore, clique potentials (Markov random field modeling for spatial constraints) is unnecessary in this step.An empirical observation was that by including clique potentials in this step, more non-bone pixels were classified as foreground.
- The skull is a contiguous tissue, so non-contiguous pixels are very unlikely to be bone. Eliminate them after each pass.

2) Second Pass:

- Bone pixels appear considerably brighter than fat in the self-normalized UTE image volume I5. However, noise pixels can appear bright too due to divide by 0 erroneous values. To eliminate these noise pixels, a 'foreground' mask is obtained from Pass 1
- After noise and brain/muscle tissue are eliminated in Pass 1, the remaining distribution is bimodal.A 2 class segmentation with Gaussian mixture model yields desirable results
- Since there is a small overlap between the bone and fat distributions, clique potentials(Markov random field based spatial constrain modeling) helps in segmenting dimmer bone pixels from brighter fat pixels. Since skull is a contiguous object, nearest-neighbor weighting is particularly well suited to this anatomical situation.

Chapter 4

Results

4.1 UTE MR Skull Segmented vs CT Ground Truth

For obtaining overlap, we consider the logical mask obtained from CT data where a threshold of 750 Hounsfield unit was applied to ensure bone appears distinct. The cranium map extracted from our algorithm was converted to a binary mask.
The results obtained are shown in Fig 4.2, 4.3, 4.4, 4.5, 4.6, 4.7, 4.8. The following index represents the anatomy shown with the overlap maps

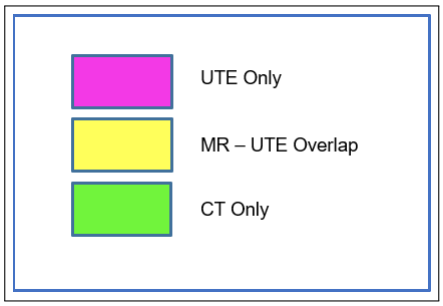

FIGURE 4.1: Visual Index for Overlap map

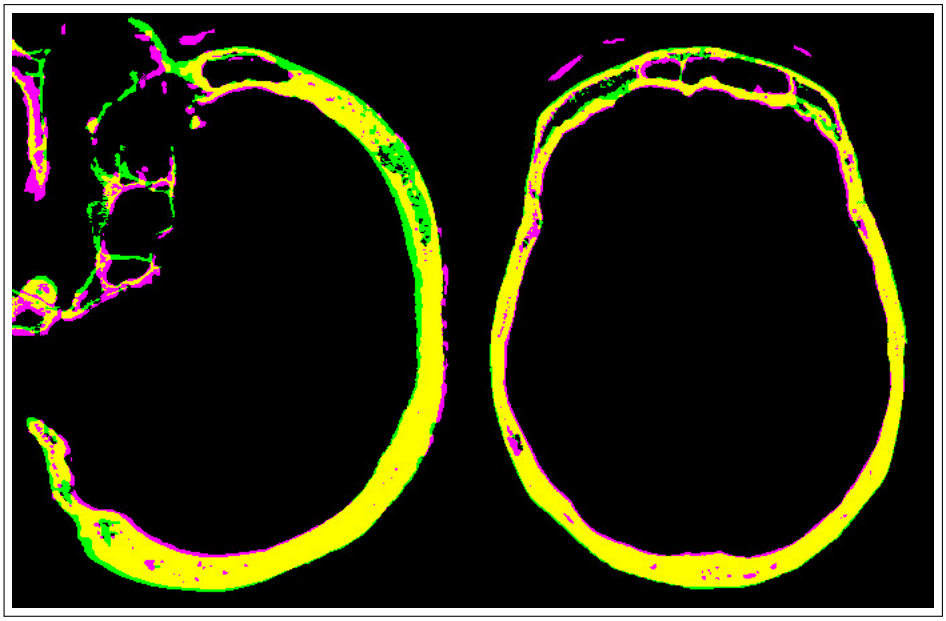

FIGURE 4.2: Subject 1 Sagittal and Axial Slice Overlap map

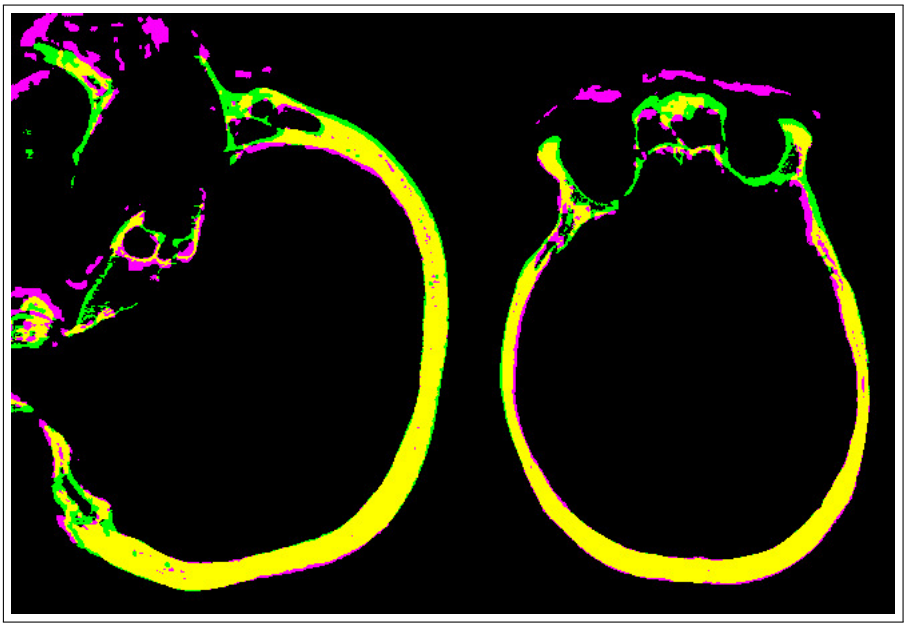

FIGURE 4.3: Subject 2 Sagittal and Axial Slice Overlap map

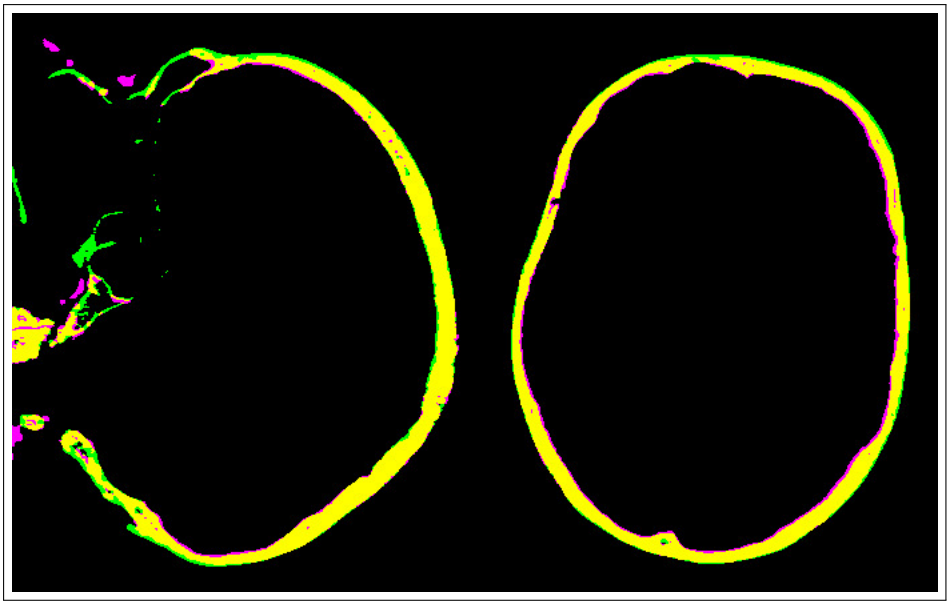

FIGURE 4.4: Subject 3 Sagittal and Axial Slice Overlap map

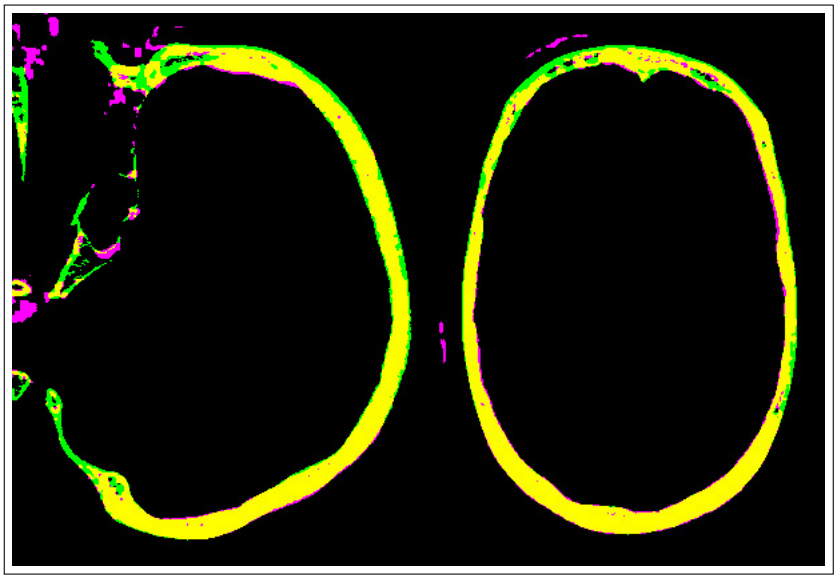

FIGURE 4.5: Subject 4 Sagittal and Axial Slice Overlap map

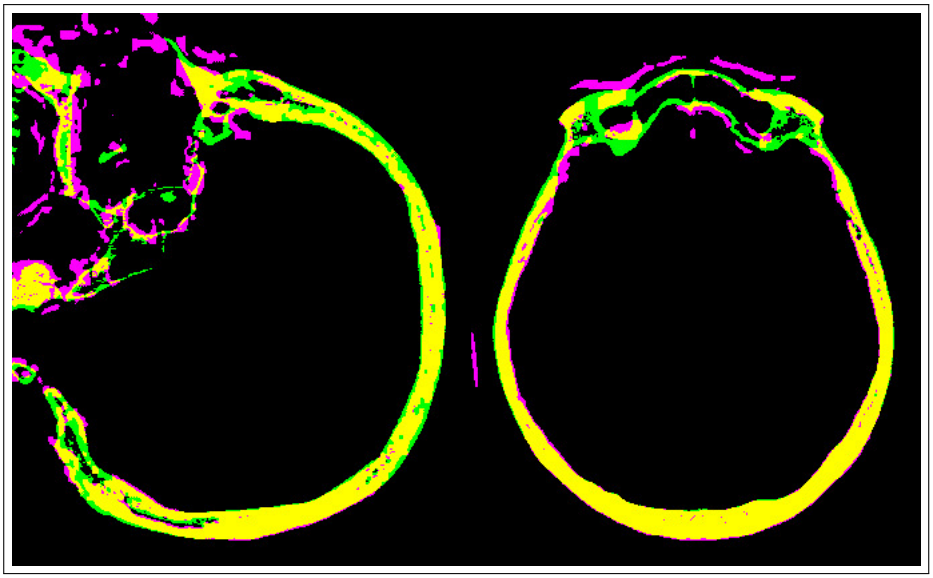

FIGURE 4.6: Subject 5 Sagittal and Axial Slice Overlap map

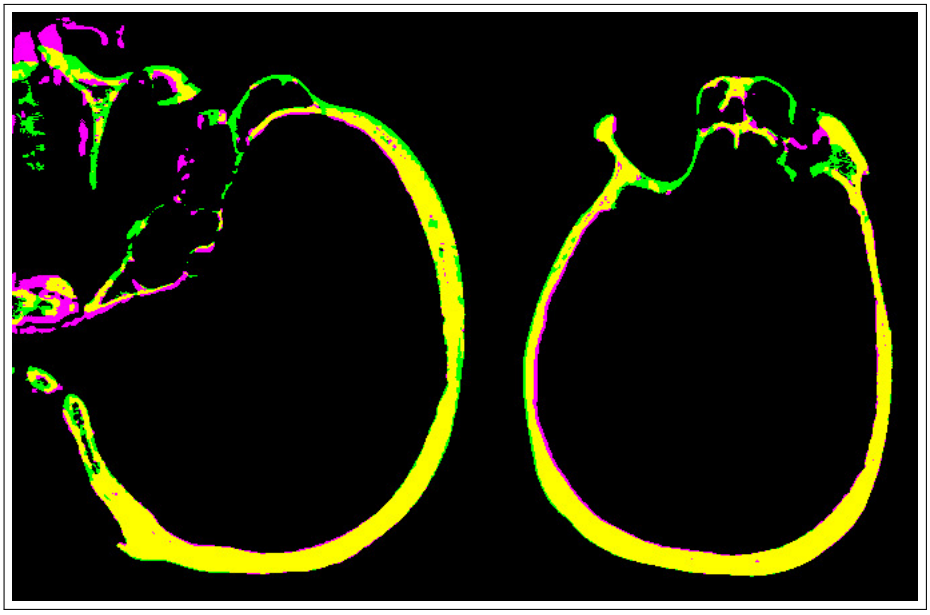

FIGURE 4.7: Subject 6 Sagittal and Axial Slice Overlap map

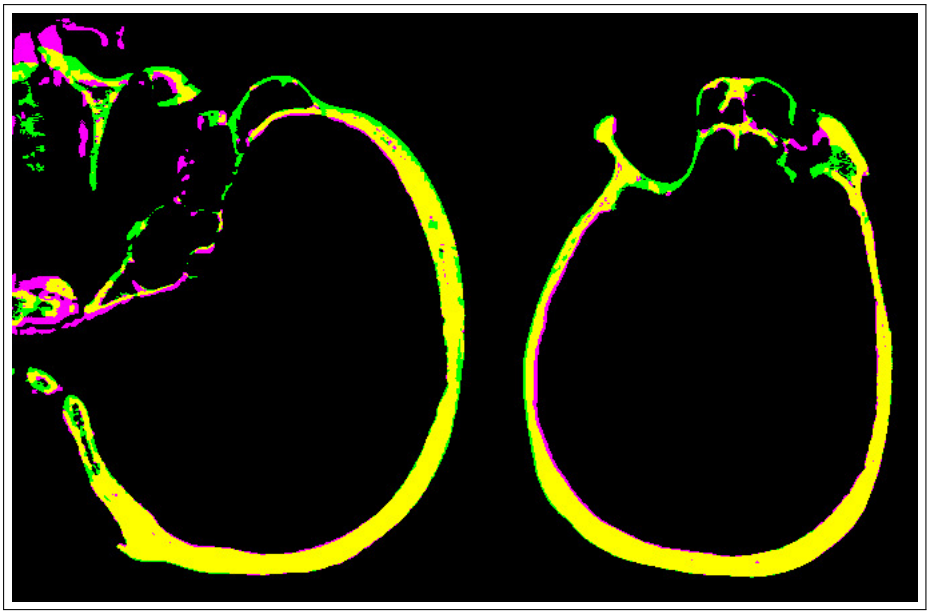

FIGURE 4.8: Subject 7 Sagittal and Axial Slice Overlap map

Yellow pixels are overlap, magenta are MR only, green are CT only. While these are only some slices from the volumetric segmentation obtained, we shall present DICE Coefficients to show overlap extent with CT ground truth in the following section.

4.2 DICE Coefficients and Runtime Metrics

Sørensen-Dice similarity coefficient for image segmentation were calculated between UTE MR based cranium segmentation and CT volume thresholded at 750 Hounsfield Unit using MATLAB's built in 'dice' function. Runtime metrics were also recorded for Pass 1 and Pass 2 of the algorithm (Pass 1 and Pass 2 are two parts of the algorithm as shown in Flowchart 3.2).

Subject number	Volume Size	DICE Score	Total Runtime (in minutes) (10 iterations Pass1+ 15 iterations Pass2)
1	446 x 353 x 338	0.74	6.36
2	450 x 315 x 347	0.76	5.55
3	434 x 342 x 352	0.81	6.23
4	414 x 292 x 317	0.81	3.30
5	414 x 340 x 341	0.72	6.20
6	441 x 320 x 359	0.79	6.21
7	452 x 332 x 350	0.77	6.11

FIGURE 4.9: DICE Score comparison between UTE MR cranium segmentation vs thresholded CT groundtruth.

The range of DICE scores available were from 0.721 to 0.817, with subject 4 dataset performing the best. We believe the DICE scores are being impacted by low fidelity in the neck and face region of the head, which do not matter for tcMRgFUS, thereby providing an opportunity for further improvement by carefully selecting the FOV for the subject volume, ignoring neck and face.

4.3 Algorithm Performance Metrics

Our metric for performance of our algorithm was the rate of convergence of the segmentation to a steady state value. It was observed that for majority of the subjects(5 out of 7), the algorithm allowed for voxel flips reducing to approximately 0 for Pass 1 in about 13 iterations. However for Pass 2, the voxel flips did not reduce to approximately 0, but stabilized around the 13th iteration.

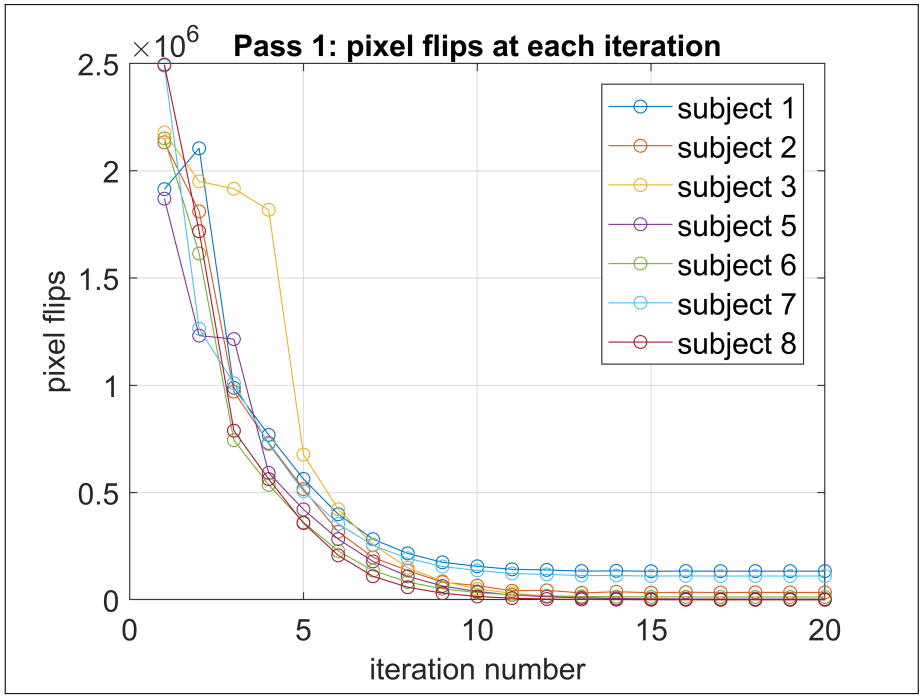

FIGURE 4.10: Plot of voxel flips/iteration for Pass 1. The voxel flips stabilize around 10th iteration

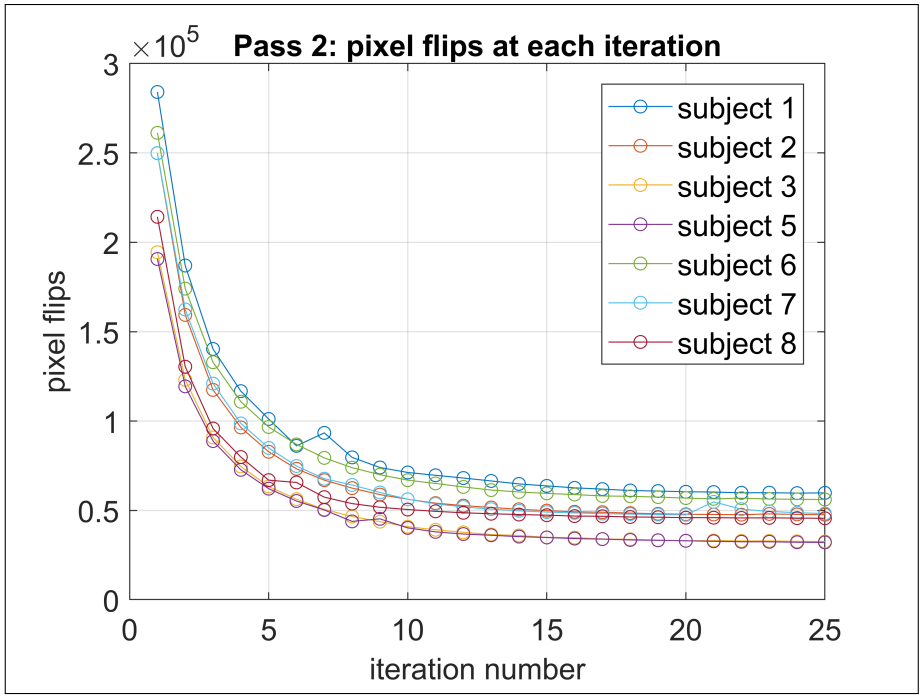

FIGURE 4.11: Plot of voxel flips/iteration for Pass 2. Unlike pass 1, the voxel flips stabilize at approximately 50,000 voxels

Chapter 5

Discussion

A custom, iterative segmentation algorithm has been demonstrated that builds on stochastic image models , with the following features and capabilities

- Operations performed on a single-contrast image (although could be modified to apply to multi-contrast images, was not necessary for this situation, due to two-pass structure of the algorithm)
- A hard segmentation is performed (not fuzzy). However, if need be, a fuzzifer can be easily introduced in this model based on the concepts presented in [22]. This may account for intravoxel signal differentiation
- Assumes that a multiplicative smoothly varying spatial field $B(\mathbf{r}_f)$ distorts optimal image $J(\mathbf{r}_f)$. This is represented in Equation 3.1 The optimal image is piecewise constant and is composed of K tissue types.
- Assumes distribution of bias-corrected pixel intensities within each class is Gaussian
- Bias field estimation and clique potential introduction can be switched on and off based on the code design
- Using UTE MR images, it is possible to generate DICE coefficients of 0.75-0.85 when compared to CT registered ground truth data.

A brief yet concise reference for Markov Random Field and stochastic image models is provided in [24].
As Miller et al. disucssed in [25], sonication using MRgFUS systems was significantly improved when the cranium presence was corrected for by utilizing manual thresholding algorithm – which allowed the researcher to get a DICE coefficient of 0.8-0.9 with co-registered CT data.Our current algorithm performs at par with this paper, while being automated. While at this moment , we are unable to differentiate between cancellous(trabecular) and cortical bone to calculate SDR, we demonstrate the working of this algorithm over multiple slices and show this holds promise for assisting in tcMRgFUS procedures. Synthetic CT volume images may be generated succesfully with a bone map when this automated skull segmentation algorithm is combined with Ultra Short Echo time MR imaging, thereby improving the clinical workflow for MRgFUS patients.

Chapter 6

Limitations and Future Work

While this algorithm has been demonstrated to perform with reasonable accuracy on UTE MR data co-registered with CT ground truth for comparison, only seven subjects were tested. By incorporating more medical image datasets, the robustness of this algorithm could be tested. At this moment, the algorithm takes approximately five minutes to execute over a volume of size 446 x 353 x 338. Incorporation of parallelization on a computer with higher computing power could potentially reduce this further. Dice coefficients could be further improved if the data is ignored neck and face region of the patient (since tcMRgFUS is concerned with the neurocranium for energy absorption and beam aberration). There is also an opportunity for MR pulse sequence development in order to quantify the differences between cortical and cancellous bones in the skull, which form the basis of the SDR. This could be done by utilizing the subtle differences in the T2* of these bone tissues. Sensitivity analysis of the algorithm with respect to each variable in the energy function depicted in Equation 3.4 may prove valuable in an attempt to have the complete automated algorithm implemented on a MRgFUS system in real time.
The Mumford-Shah model for image segmentation combined with a deep learning approach with unsupervised learning [26] also holds immense value for this particular research, thanks to the advent in computational resources and deep learning networks. It is a research area that definitely commends further exploration specifically to skull segmentation using UTE MRI.

Bibliography

[1] F. A. Jolesz, "MRI-Guided Focused Ultrasound Surgery", en, *Annual Review of Medicine*, vol. 60, no. 1, pp. 417–430, Feb. 2009, ISSN: 0066-4219, 1545-326X. DOI: 10.1146/annurev.med.60.041707.170303. [Online]. Available: http://www.annualreviews.org/doi/10.1146/annurev.med.60.041707.170303 (visited on 08/03/2020).

[2] P. Ghanouni, K. B. Pauly, W. J. Elias, J. Henderson, J. Sheehan, S. Monteith, and M. Wintermark, "Transcranial MRI-Guided Focused Ultrasound: A Review of the Technologic and Neurologic Applications", en, *American Journal of Roentgenology*, vol. 205, no. 1, pp. 150–159, Jul. 2015, ISSN: 0361-803X, 1546-3141. DOI: 10.2214/AJR.14.13632. [Online]. Available: http://www.ajronline.org/doi/10.2214/AJR.14.13632 (visited on 08/03/2020).

[3] N. Lipsman, T. G. Mainprize, M. L. Schwartz, K. Hynynen, and A. M. Lozano, "Intracranial Applications of Magnetic Resonance-guided Focused Ultrasound", en, *Neurotherapeutics*, vol. 11, no. 3, pp. 593–605, Jul. 2014, ISSN: 1933-7213, 1878-7479. DOI: 10.1007/s13311-014-0281-2. [Online]. Available: http://link.springer.com/10.1007/s13311-014-0281-2 (visited on 08/03/2020).

[4] K. Hynynen and G. Clement, "Clinical applications of focused ultrasound—The brain", en, *International Journal of Hyperthermia*, vol. 23, no. 2, pp. 193–202, Jan. 2007, ISSN: 0265-6736, 1464-5157. DOI: 10.1080/02656730701200094. [Online]. Available: http://www.tandfonline.com/doi/full/10.1080/02656730701200094 (visited on 08/03/2020).

[5] A. L. Crowell, P. Riva-Posse, P. E. Holtzheimer, S. J. Garlow, M. E. Kelley, R. E. Gross, L. Denison, S. Quinn, and H. S. Mayberg, "Long-Term Outcomes of Subcallosal Cingulate Deep Brain Stimulation for Treatment-Resistant Depression", en, *American Journal of Psychiatry*, vol. 176, no. 11, pp. 949–956, Nov. 2019, ISSN: 0002-953X, 1535-7228. DOI: 10.1176/appi.ajp.2019.18121427. [Online]. Available: http://ajp.psychiatryonline.org/doi/10.1176/appi.ajp.2019.18121427 (visited on 08/03/2020).

[6] *Overview - Focused Ultrasound Foundation*. [Online]. Available: https://www.fusfoundation.org/diseases-and-conditions/overview (visited on 08/03/2020).

[7] *Focused Ultrasound | UVA Health*. [Online]. Available: https://uvahealth.com/services/focused-ultrasound (visited on 08/03/2020).

[8] F. J. Fry and J. E. Barger, "Acoustical properties of the human skull", en, *The Journal of the Acoustical Society of America*, vol. 63, no. 5, pp. 1576–1590, May 1978, ISSN: 0001-4966. DOI: 10.1121/1.381852. [Online]. Available: http://asa.scitation.org/doi/10.1121/1.381852 (visited on 08/03/2020).

[9] A. Kyriakou, E. Neufeld, B. Werner, M. M. Paulides, G. Szekely, and N. Kuster, "A review of numerical and experimental compensation techniques for skull-induced phase aberrations in transcranial focused ultrasound", en, *International Journal of Hyperthermia*, vol. 30, no. 1, pp. 36–46, Feb. 2014, ISSN: 0265-6736, 1464-5157. DOI: 10.3109/02656736.2013.861519. [Online]. Available: http://www.tandfonline.com/doi/full/10.3109/02656736.2013.861519 (visited on 08/03/2020).

[10] A. Boutet, D. Gwun, R. Gramer, M. Ranjan, G. J. B. Elias, D. Tilden, Y. Huang, S. X. Li, B. Davidson, H. Lu, P. Tyrrell, R. M. Jones, A. Fasano, K. Hynynen, W. Kucharczyk, M. L. Schwartz, and A. M. Lozano, "The relevance of skull density ratio in selecting candidates for transcranial MR-guided focused ultrasound", *Journal of Neurosurgery*, vol. 132, no. 6, pp. 1785–1791, Jun. 2020, ISSN: 0022-3085, 1933-0693. DOI: 10.3171/2019.2.JNS182571. [Online]. Available: https://thejns.org/view/journals/j-neurosurg/132/6/article-p1785.xml (visited on 08/03/2020).

[11] W. S. Chang, H. H. Jung, E. Zadicario, I. Rachmilevitch, T. Tlusty, S. Vitek, and J. W. Chang, "Factors associated with successful magnetic resonance-guided focused ultrasound treatment: Efficiency of acoustic energy delivery through the skull", *Journal of Neurosurgery*, vol. 124, no. 2, pp. 411–416, Feb. 2016, ISSN: 0022-3085, 1933-0693. DOI: 10.3171/2015.3.JNS142592. [Online]. Available: https://thejns.org/view/journals/j-neurosurg/124/2/article-p411.xml (visited on 08/03/2020).

[12] E. Y. Chang, J. Du, and C. B. Chung, "UTE imaging in the musculoskeletal system: UTE Imaging in the MSK System", en, *Journal of Magnetic Resonance Imaging*, vol. 41, no. 4, pp. 870–883, Apr. 2015, ISSN: 10531807. DOI: 10.1002/jmri.24713. [Online]. Available: http://doi.wiley.com/10.1002/jmri.24713 (visited on 08/03/2020).

[13] E. Zadicario, "ExAblate neuro transcranial treatment considerations", en, *Journal of Therapeutic Ultrasound*, vol. 3, no. S1, O33, Dec. 2015, ISSN: 2050-5736. DOI: 10.1186/2050-5736-3-S1-O33. [Online]. Available: https://jtultrasound.biomedcentral.com/articles/10.1186/2050-5736-3-S1-O33 (visited on 08/03/2020).

[14] "Fast imaging in the steady state", in *Magnetic Resonance Imaging*. John Wiley Sons, Ltd, 2014, ch. 18, pp. 447–510, ISBN: 9781118633953. DOI: 10.1002/9781118633953.ch18. eprint: https://onlinelibrary.wiley.com/doi/pdf/10.1002/9781118633953.ch18. [Online]. Available: https://onlinelibrary.wiley.com/doi/abs/10.1002/9781118633953.ch18.

[15] M. R. Mitchell, R. W. Tarr, T. E. Conturo, C. L. Partain, and A. E. James, "Spin echo technique selection: Basic principles for choosing MRI pulse sequence timing intervals.", en, *RadioGraphics*, vol. 6, no. 2, pp. 245–260, Mar. 1986, ISSN: 0271-5333, 1527-1323. DOI: 10.1148/radiographics.6.2.3685491. [Online]. Available: http://pubs.rsna.org/doi/10.1148/radiographics.6.2.3685491 (visited on 08/04/2020).

[16] E. R. McVeigh, M. J. Bronskill, and R. M. Henkelman, "Phase and sensitivity of receiver coils in magnetic resonance imaging", *Medical physics*, vol. 13, no. 6, pp. 806–814, 1986, ISSN: 0094-2405. [Online]. Available: https://www.ncbi.nlm.nih.gov/pmc/articles/PMC2396267/ (visited on 08/04/2020).

[17] J. Sled, A. Zijdenbos, and A. Evans, "A nonparametric method for automatic correction of intensity nonuniformity in MRI data", *IEEE Transactions on Medical Imaging*, vol. 17, no. 1, pp. 87–97, Feb. 1998, ISSN: 02780062. DOI: 10.1109/42.668698. [Online]. Available: http://ieeexplore.ieee.org/document/668698/ (visited on 08/03/2020).

[18] B. Belaroussi, J. Milles, S. Carme, Y. M. Zhu, and H. Benoit-Cattin, "Intensity non-uniformity correction in MRI: Existing methods and their validation", en, *Medical Image Analysis*, vol. 10, no. 2, pp. 234–246, Apr. 2006, ISSN: 13618415. DOI: 10.1016/j.media.2005.09.004. [Online]. Available: https://linkinghub.elsevier.com/retrieve/pii/S1361841505000976 (visited on 08/04/2020).

[19] U. Vovk, F. Pernus, and B. Likar, "A Review of Methods for Correction of Intensity Inhomogeneity in MRI", *IEEE Transactions on Medical Imaging*, vol. 26, no. 3, pp. 405–421, Mar. 2007, ISSN: 0278-0062. DOI: 10.1109/TMI.2006.891486. [Online]. Available: http://ieeexplore.ieee.org/document/4114560/ (visited on 08/03/2020).

[20] Y. Zhang, M. Brady, and S. Smith, "Segmentation of brain MR images through a hidden Markov random field model and the expectation-maximization algorithm", *IEEE Transactions on Medical Imaging*, vol. 20, no. 1, pp. 45–57, Jan. 2001, ISSN: 02780062. DOI: 10.1109/42.906424. [Online]. Available: http://ieeexplore.ieee.org/document/906424/ (visited on 08/03/2020).

[21] N. J. Tustison, B. B. Avants, P. A. Cook, Yuanjie Zheng, A. Egan, P. A. Yushkevich, and J. C. Gee, "N4ITK: Improved N3 Bias Correction", *IEEE Transactions on Medical Imaging*, vol. 29, no. 6, pp. 1310–1320, Jun. 2010, ISSN: 0278-0062, 1558-254X. DOI: 10.1109/TMI.2010.2046908. [Online]. Available: http://ieeexplore.ieee.org/document/5445030/ (visited on 08/03/2020).

[22] C. Li, J. C. Gore, and C. Davatzikos, "Multiplicative intrinsic component optimization (MICO) for MRI bias field estimation and tissue segmentation", en, *Magnetic Resonance Imaging*, vol. 32, no. 7, pp. 913–923, Sep. 2014, ISSN: 0730725X. DOI: 10.1016/j.mri.2014.03.010. [Online]. Available: https://linkinghub.elsevier.com/retrieve/pii/S0730725X14000927 (visited on 08/03/2020).

[23] J. Besag, "Spatial Interaction and the Statistical Analysis of Lattice Systems", en, *Journal of the Royal Statistical Society: Series B (Methodological)*, vol. 36, no. 2, pp. 192–225, Jan. 1974, ISSN: 00359246. DOI: 10.1111/j.2517-6161.1974.tb00999.x. [Online]. Available: http://doi.wiley.com/10.1111/j.2517-6161.1974.tb00999.x (visited on 08/03/2020).

[24] C. Bouman, *Markov Random Fields and Stochastic Image Models*. [Online]. Available: https://engineering.purdue.edu/~bouman/publications/tutorials/mrf_tutorial/references.pdf.

[25] G. W. Miller, M. Eames, J. Snell, and J.-F. Aubry, "Ultrashort echo-time MRI versus CT for skull aberration correction in MR-guided transcranial focused ultrasound: *In vitro* comparison on human calvaria: UTE-based skull aberration correction for MR-guided HIFU", en, *Medical Physics*, vol. 42, no. 5, pp. 2223–2233, Apr. 2015, ISSN: 00942405. DOI: 10.1118/1.4916656. [Online]. Available: http://doi.wiley.com/10.1118/1.4916656 (visited on 08/03/2020).

[26] B. Kim and J. C. Ye, "Mumford–shah loss functional for image segmentation with deep learning", *IEEE Transactions on Image Processing*, vol. 29, pp. 1856–1866, 2020. DOI: 10.1109/TIP.2019.2941265.